Current Science
CS 5 (2), 1592-1603 (2025)
Received 10 **Dec** 2024 | **Revised 22 Jan** 2025 | **Accepted 20 Feb**. 2025 | **Online Available 18 March** 2025
https://doi.org/ 10.52845/CS/2025-5-2-24

Current Science

Current Science

OPEN ACCESS

ISSN(O)2795-8639

ORIGINAL ARTICLE

Torsional Vibration Analysis of Nonlinear Model for Equipment Driveline System

Hongyan Wang[a,b], Yu Qu[b], Liping Tan[c], Chao Liu[a,b*], Jian Liu[b], Junguo Cui[b*], Chengzhi Xue[d], Yaqi Chen[e]

[a]College of Electromechanical Engineering, Qingdao University of Science & Technology, Qingdao 266061, China

[b]National Engineering Research Center of Marine Geophysical Prospecting and Exploration and Development Equipment, China University of Petroleum (East China), Qingdao 266580, China

[C]ulsan Ship and Ocean College Ludong University, Yantan, China

[d]Xuzhou Construction Machinery Group, Xuzhou 221004, China

[e]Weichai Power Co., Ltd., Weifang 261061, China

[*]Corresponding Author: Chao Liu, Junguo Cui

Abstract

In recent years, the exploitation of unconventional natural gas resources, such as coalbed methane and shale gas, along with the continuous promotion of measures to enhance production from existing oil and gas fields, has significantly increased the demands on oil and gas fracturing equipment. The torsional vibration of the transmission system in such equipment can critically affect its performance and service life. This study focuses on the transmission system of a specific type of fracturing truck. A nonlinear dynamic model of the transmission system is established, incorporating time-varying meshing stiffness, time-varying meshing damping, comprehensive meshing error, and tooth side clearance as nonlinear parameters for each gear pair. The nonlinear torsional vibration response is solved using the fourth-order Runge-Kutta method with adaptive step size, revealing a maximum torsional vibration angle of 0.5863° in the transmission system. Furthermore, a qualitative analysis of the nonlinear system is conducted, yielding bifurcation diagrams, phase plane diagrams, and Poincaré cross-section diagrams based on the damping coefficient to explore the stability and periodicity of the nonlinear system solutions. The developed nonlinear model of the fracturing equipment's transmission system provides valuable insights for enhancing system stability and improving the accuracy of torsional vibration simulation analyses.

Keywords: fracturing truck, drive train, torsional vibration, nonlinear analysis

Introduction

The increasing demand for oil and gas extraction, driven by the exploitation of unconventional resources such as coalbed methane and shale gas, has spurred significant advancements in hydraulic fracturing technologies. A key factor in the performance of fracturing equipment, particularly fracturing trucks, is the effectiveness of their driveline systems, especially the transmission components. These systems are essential for transmitting power from the engine to the operational components, often subjecting them to substantial torsional vibrations. Such vibrations not only affect operational efficiency but also have critical implications for the durability and reliability of driveline components. As a result, understanding and mitigating torsional vibrations in fracturing truck driveline systems has become a key focus of recent research.

Torsional vibration has been a longstanding challenge in driveline systems. To analyze its mechanisms and control strategies, researchers worldwide have proposed various analytical approaches. Liu et al. [1] developed a dynamic equation for a two-mass nonlinear torsional vibration system with tooth clearance, deriving an exact solution using the multiple scales method. They explored the effect of tooth clearance variations on the torsional response. Li et al. [2] proposed a nonlinear vibration amplitude model, considering clutch stick-slip characteristics, and derived the torsional vibration response analytically, analyzing the self-excited vibration behavior of the clutch's driven plate. Wang et al. [3] established a nonlinear dynamic model for the GTF engine's star gear-rotor coupling transmission system, incorporating time-varying meshing stiffness, error, and tooth clearance as piecewise nonlinear parameters. Using the Runge-Kutta method, they examined the effects of key parameters such as input speed, tooth side clearance, meshing error, and gear meshing damping on the torsional response. Qu et al. [4] studied the influence of clutch nonlinearities on torsional vibration in automotive drivelines using numerical simulations and experimental validation. They developed a seven-degree-of-freedom powertrain model that considers transient engine torque, multi-stage clutch nonlinearities, and tire slip to analyze the dynamic behaviors of the driveline system. Moharrami et al. [5] introduced an efficient finite element modeling approach to simulate stick-slip torsional vibrations in full drill strings, including rate-dependent bit-rock interaction, frictional contact, large rotation nonlinearities, and axial-torsional coupling. They validated their five-degree-of-freedom lumped parameter model with field test comparisons, demonstrating its ability to capture self-excited torsional vibrations at frequencies lower than the first natural frequency of the drill string. Xia et al. [6-8] developed a nonlinear dynamic model of a pickup truck driveline system, incorporating new elements such as a general nonlinear clearance element, a friction element with the Stribeck effect, and a nonlinear multi-stage stiffness-damping element. They established a 10-degree-of-freedom lumped parameter model and numerically studied transient vibro-impact, stick-slip, and hysteresis phenomena during clutch engagement, with experimental validation. Idehara et al. [9] used bench test results for torsional dampers and powertrain vibration measurements to calibrate a nonlinear three-degree-of-freedom model, estimating driveline natural frequency and time-response vibrations, employing order tracking to isolate engine excitation responses. He et al. [10] developed and simulated an analytical model of a dual-mass flywheel (DMF) driveline torsional vibration system during engine start-up, analyzing driveline excitation and comparing simulation results with vehicle start-up tests. The study further investigated the effects of DMF parameters, such as rotary inertia ratio, hysteresis torque, and nonlinear torsional stiffness, on vibration attenuation, and proposed DMF design requirements for optimal performance during start-up.

Despite significant progress in the study of torsional vibrations in driveline systems, research focusing specifically on the nonlinear dynamics of fracturing truck transmission systems remains limited. With the development of artificial intelligence technology, it has driven the advancement of the field of mechanical engineering [11-20]. This study aims to address this gap by developing a comprehensive nonlinear model of the driveline system in fracturing trucks, incorporating key nonlinear parameters such as time-varying meshing stiffness, damping, and tooth side clearance. The proposed model provides a more accurate representation of the system's dynamic behavior, offering valuable insights into the stability and performance characteristics of fracturing truck transmission systems.

2 Modelling of non-linear systems

2.1 Time-varying meshing stiffness of gears

The specific expression for stiffness is shown in Eq. (1).

$$K = \frac{F}{L\delta_0} \tag{1}$$

in which, F is the load acting on the normal plane; L is the face width of the gear teeth; δ_0 is the total amount of tooth deformation.

Total deformation of the gear in the direction of the meshing line at the point of loading δ_0 can be

derived from Eq. (2).

$$\delta_0=\delta_{Br}+\delta_{Bt}+\delta_S+\delta_G \tag{2}$$

δ_{Br} is the deformation of the rectangle in the simplified model, can be derived from Eq. (3).

$$\delta_{Br}=\frac{12F_N\cos^2\omega_x}{EbS_f^3}\left[h_xh_r\left(h_x-h_r\right)+\frac{h_r^3}{3}\right] \tag{3}$$

δ_{Bt} is the deformation of the trapezoidal part of the simplified model, can be derived from Eq. (4).

$$\delta_{Bt}=\frac{6F_N\cos^2\omega_x}{EbS_f^3}\left(h_i-h_r\right)^3\left[\frac{h_i-h_x}{h_i-h_r}\left(4-\frac{h_i-h_x}{h_i-h_r}\right)-2\ln\frac{h_i-h_x}{h_i-h_r}-3\right] \tag{4}$$

δ_S is the amount of deformation produced by the shear force, can be derived from Eq. (5).

$$\delta_S=\frac{2\left(1+\nu\right)F_N\cos^2\omega_x}{EbS_f}\left[h_r+\left(h_i-h_r\right)\ln\frac{h_i-h_r}{h_i-h_x}\right] \tag{5}$$

δ_G is the elastic deformation caused by the inclination of the tooth root base, can be derived from Eq. (6).

$$\delta_G=\frac{24F_Nh_x^2\cos^2\omega_x}{\pi EbS_f^2} \tag{6}$$

When the gears mesh, the total deformation between the gear pairs δ_Σ,can be derived from Eq. (7).

$$\delta_\Sigma=\delta_1+\delta_2+\delta_{pv} \tag{7}$$

in which, δ_1、 δ_2 are the deformation of a single gear in the direction of the meshing line; δ_{pv} is the amount of deformation of the contact part of the tooth surface, can be derived from Eq. (8).

$$\delta_{pv}=\frac{4\left(1-\nu^2\right)}{\pi E}\frac{F_N}{b} \tag{8}$$

Since the time-varying meshing stiffness exhibits periodicity, it can be fitted to a Fourier series, the time-varying engagement stiffness obtained $k_m\left(t\right)$ is shown in Eq. (9).

$$k_m\left(t\right)=k_0+\sum_{z=1}^{n}\left[a_z\cos\left(z\omega_mt\right)+b_z\sin\left(z\omega_mt\right)\right] \tag{9}$$

in which, $k_m\left(t\right)$is the time-varying engagement stiffness; k_0 is the Fourier series constant term; $a_z$is the Fourier series cosine term; b_z is the Fourier series sine term; ω_m is the gear meshing frequency.

The relationship between the fitting error of the Fourier series expansion and the number of expansion orders is obtained using MATLAB and is shown in Fig. 1. The Fourier series expansion order with the smallest error degree is obtained as 10th order, and the time-varying stiffness of the gear fitted by 10th order Fourier series is shown in Fig. 2.

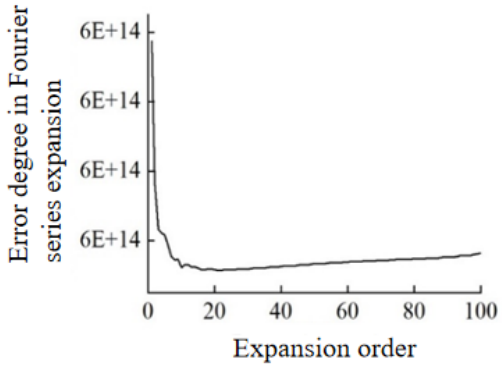

Figure 1 Fitting error of Fourier series

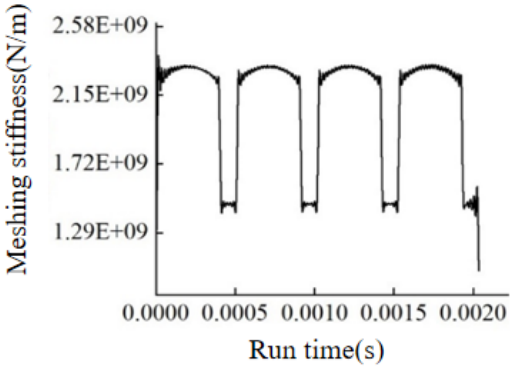

Figure 2 Fitting curve of Fourier series

2.2 Time-varying gear mesh damping

Gear mesh damping is proportional to the time-varying mesh stiffness of the gear, and since the mesh stiffness has a time-varying characteristic, the mesh damping also has a time-varying characteristic [13]. The method of analyzing gear dynamics that locates the mesh damping as a constant is not rigorous, and the time-varying mesh damping can be derived from Eq. (10).

$$C_m(t) = 2\xi\sqrt{k_m(t)\frac{J_1 J_2 r_{b1}^2 r_{b2}^2}{r_{b1}^2 J_1 + r_{b2}^2 J_2}} \qquad (10)$$

in which, J_1, J_2 are the moment of inertia of the master and slave gears respectively; $k_m(t)$ is the time-varying engagement stiffness; r_{b1}, r_{b2} are the radii of the base circle of the master and slave gears respectively; $C_m(t)$ is the time-varying engagement damping; ξ is the damping ratio, which ranges from 0.03 to 0.17, and 0.1 is taken in this paper.

The time-varying meshing damping of the gears is shown in Fig. 3.

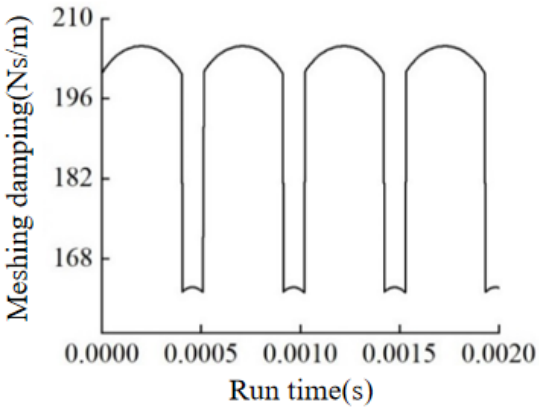

Figure 3 Time-varying meshing damping of gear

2.3 Combined gear mesh error

The meshing errors of gears are generally due to gear machining and assembly deviations and are one of the main dynamic excitations affecting the meshing operation of gears. It mainly consists of tooth shape error and base pitch error, and in the theory of gear dynamics, the cause of these errors can be understood as the wheel tooth meshing error that exists between the actual tooth profile and the ideal tooth profile. Let the gear tooth meshing error be a cyclic error, which can be expressed by a sinusoidal function as Eq. (11).

$$e(t) = e_0 + e_r \sin(2\pi t/T_z + \varphi) \qquad (11)$$

in which, e_0 is a constant value for the combined meshing error of the gear teeth. Usually taken as $e_0 = 0$; e_r is the magnitude of the combined meshing error of the gear teeth, can be selected according to the modulus of the gear, the number of teeth and processing accuracy to consult GB/T

10095.1-2001; T_z is the meshing period of the gear, $T_z = 60/nz$, where n is the gear speed and z is the number of gear teeth.

In gear transmission systems, a certain lubrication gap must be maintained between the tooth profiles to reduce friction between the gear teeth. Due to the presence of tooth side clearance, gear meshing leads to phenomena such as tooth surface disengagement and tooth back contact. Along the meshing line Q of the gear pair, the state of the tooth mesh varies within the interval [0, $2b_i$], where b_i represents half of the tooth side clearance. The relative displacement of the gear teeth along the meshing line is described by Eq. (12), which is a discontinuous, non-differentiable, and highly nonlinear function, as illustrated in Fig. 4.

$$f(\delta_i) = \begin{cases} \delta_i - b_i & \delta_i > b_i \\ 0 & |\delta_i| \le b_i \\ \delta_i + b_i & \delta_i < -b_i \end{cases} \quad (12)$$

in which, δ_i is the relative displacement on the meshing line of the gear pair; b_i is 1/2 tooth side clearance.

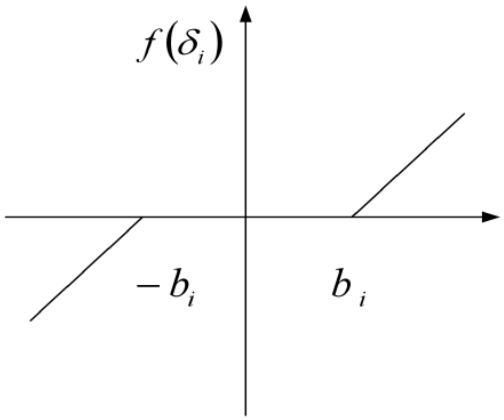

Figure 4 Nonlinear function of tooth side clearance

Based on the above nonlinear parameters, the analytical model of gear dynamics within the drive train is shown in Fig. 5. J_{in}、θ_{in}、r_{bin} are the moment of inertia, angle of rotation and radius of the base circle of the main wheel, respectively; J_{out}、θ_{out}、r_{bout} are the moment of inertia, angle of rotation and radius of the base circle of the driven wheel, respectively; $k_m(t)$ is the time-varying meshing stiffness of the gear; $c_m(t)$ is the time-varying meshing damping of the gears; $e(t)$ is the combined gear meshing error; $2b_i$ is the tooth side clearance.

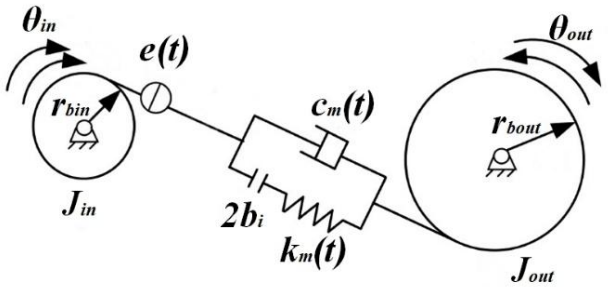

Figure 5 Dynamic model of gear system

The relative linear displacement between the two meshing gears can be derived from Eq. (13) due to the effect of non-linear parameters such as the

combined gear meshing error and tooth side clearance.

$$u_i = \left(u_{out} - u_{in} + e(t) + f\left(\delta_i\right)\right) \quad (13)$$

The tangential force between the two meshing gears subjected to time-varying meshing stiffness can be derived from Eq. (14).

$$F_{ki} = k_m(t) \cdot u_i \quad (14)$$

Similarly, the tangential force due to the time-varying engagement damping can be derived from Eq. (15).

$$F_{ci} = c_m(t) \cdot \dot{u}_i \quad (15)$$

In this way, the equation of the active wheel dynamics in the drive train is Eq. (16).

$$J_{in}\ddot{\theta}_{in} - F_{ki} r_{bin} - F_{ci} r_{bin} = T_{in} \quad (16)$$

The dynamic equation of the driven wheel is Eq. (17).

$$J_{out}\ddot{\theta}_{out} + F_{ki} r_{bout} + F_{ci} r_{bout} = T_{out} \quad (17)$$

The nonlinear dynamic equation for the drive train of the equipment on the integral fracturing truck table is Eq. (18).

$$\mathbf{J}\ddot{\boldsymbol{\theta}} + \mathbf{C}\dot{\boldsymbol{\theta}} + \mathbf{K}\boldsymbol{\theta} = \mathbf{T} \quad (18)$$

in which, **J** is the equivalent rotational inertia of the inertia disc of the drivetrain, **K** is the stiffness matrix of the drivetrain, **T** is the external excitation vector of the drivetrain, and C is the damping matrix of the drivetrain, with their respective expressions:

$$\mathbf{J} = \begin{bmatrix} J_1 & & & & & & \\ & J_2 & & & & & \\ & & J_3 & & & & \\ & & & \mathrm{O} & & & \\ & & & & J_{32} & & \\ & & & & & J_{33} & \\ & & & & & & J_{34} \end{bmatrix} \quad (19)$$

$$\mathbf{K} = \begin{bmatrix} k_1 & \mathrm{L} & 0 & 0 & 0 & \mathrm{L} & 0 \\ \mathrm{M} & \mathrm{M} & \mathrm{M} & \mathrm{M} & \mathrm{M} & \mathrm{M} & \mathrm{M} \\ 0 & \mathrm{L} & -k_{13} & k_{13} + k_{m3}(t) r_{b3}^2 & -k_{m4}(t) r_{b3} r_{b4} & \mathrm{L} & 0 \\ 0 & \mathrm{L} & 0 & -k_{m4}(t) r_{b3} r_{b4} & k_{15} + k_{m3}(t) r_{b4}^2 & \mathrm{L} & 0 \\ \mathrm{M} & \mathrm{M} & \mathrm{M} & \mathrm{M} & \mathrm{M} & \mathrm{M} & \mathrm{M} \\ 0 & \mathrm{L} & 0 & 0 & 0 & \mathrm{L} & k_{33} \end{bmatrix} \quad (20)$$

$$\mathbf{C} = \begin{bmatrix} c_1 & \mathrm{L} & 0 & 0 & 0 & \mathrm{L} & 0 \\ \mathrm{M} & \mathrm{M} & \mathrm{M} & \mathrm{M} & \mathrm{M} & \mathrm{M} & \mathrm{M} \\ 0 & \mathrm{L} & -c_{13} & c_{13} + c_{m3}(t) r_{b3}^2 & -c_{m4}(t) r_{b3} r_{b4} & \mathrm{L} & 0 \\ 0 & \mathrm{L} & 0 & -c_{m4}(t) r_{b3} r_{b4} & c_{15} + c_{m3}(t) r_{b4}^2 & \mathrm{L} & 0 \\ \mathrm{M} & \mathrm{M} & \mathrm{M} & \mathrm{M} & \mathrm{M} & \mathrm{M} & \mathrm{M} \\ 0 & \mathrm{L} & 0 & 0 & 0 & \mathrm{L} & c_{33} \end{bmatrix} \quad (21)$$

$$\mathbf{T}=\begin{bmatrix}0\\T_1\\T_2\\\mathrm{M}\\T_{13}\\0\\0\end{bmatrix}=\begin{bmatrix}0\\a_{10}\\a_{20}\\\mathrm{M}\\a_{130}\\0\\0\end{bmatrix}+\begin{bmatrix}0\\\sum_{i=1}^{m}a_{1i}\sin(i\omega_0 t)\\\sum_{i=1}^{m}a_{2i}\sin(i\omega_0 t)\\\mathrm{M}\\\sum_{i=1}^{m}a_{13i}\sin(i\omega_1 t)\\0\\0\end{bmatrix}+\begin{bmatrix}0\\\sum_{i=1}^{m}b_{1i}\cos(i\omega_0 t)\\\sum_{i=1}^{m}b_{2i}\cos(i\omega_0 t)\\\mathrm{M}\\\sum_{i=1}^{m}b_{13i}\cos(i\omega_1 t)\\0\\0\end{bmatrix} \quad (22)$$

3 Nonlinear response solving

The methods for solving nonlinear problems include analytical, geometric and numerical solutions. Since the gear system is more nonlinear and it is difficult to solve the problem by analytical and geometric methods, this paper adopts the fourth-order Lunger-Kutta method with adaptive step size to solve the problem. The specific formulas are shown in Eq. (23) ~ (27).

$$y_{i+1}=y_i+\frac{h}{6}\left(K_1+2K_2+2K_3+K_4\right) \quad (23)$$

$$K_1=f\left(x_i,y_i\right) \quad (24)$$

$$K_2=f\left(x_i+\frac{h}{2},y_i+\frac{h}{2}K_1\right) \quad (25)$$

$$K_3=f\left(x_i+\frac{h}{2},y_i+\frac{h}{2}K_2\right) \quad (26)$$

$$K_4=f\left(x_i+h,y_i+hK_3\right) \quad (27)$$

in which, h is the step length. Usually, the truncation error decreases as the step size decreases, but as the step size decreases, the number of steps in a certain interval also increases, which leads to the increase of workload with the large accumulation and transmission of rounding error.

The adaptive step-size Lunger-Kutta method inherits the advantage of the classical Lunger-Kutta method [16] in solving conveniently, and cleverly balances the accuracy and computational volume, so the adaptive step-size fourth-order Lunger-Kutta method is chosen in this paper for solving the response problem of nonlinear systems. The basic principle is: Starting from node x_i,the approximate value is first obtained using a step size of h,denoted by $y_{i+1}^{(h)}$,since the local truncation error of the fourth-order Longe-Kuta method is $O(h^5)$, Eq. (28) is available:

$$y\left(x_{i+1}\right)-y_{i+1}^{(h)}\approx ch^5 \quad (28)$$

When h does not change much, the coefficient c can be viewed as a constant. Reducing the step size by half, taking $h/2$ as the step size. Then from node x_i as a starting point, spanning two steps to node x_{i+1},then get an approximation $y_{i+1}^{(h/2)}$, This results in a truncation error of $c\left(h/2\right)^5$ per step across, hence Eq. (29) ~ Eq. (31).

$$y\left(x_{i+1}\right)-y_{i+1}^{(h/2)}\approx 2c\left(\frac{h}{2}\right)^5 \quad (29)$$

$$\frac{y(x_{i+1})-y_{i+1}^{(h/2)}}{y(x_{i+1})-y_{i+1}^{(h)}} \approx \frac{1}{16} \quad (30)$$

$$y(x_{i+1})-y_{i+1}^{(h/2)} \approx \frac{1}{15}\left(y_{i+1}^{(h/2)}-y_{i+1}^{(h)}\right) \quad (31)$$

The deviation of the two calculations before and after halving the step length can be used to judge whether the step length is appropriate, and the error is shown in Eq. (32)/

$$\Delta = \left|y_{i+1}^{(h/2)}-y_{i+1}^{(h)}\right| \quad (32)$$

When the required numerical accuracy is ε, it is divided into the following two cases:

When $\Delta > \varepsilon$, the step length is halved several times until $\Delta < \varepsilon$, and the calculation of its last step length is taken as y_{i+1};

When $\Delta < \varepsilon$, double the calculation for the step size several times until $\Delta > \varepsilon$, and take the result of the last step size calculation as y_{i+1}.

This method, which adjusts the step size to control the solution accuracy, is known as the adaptive step size method. Although it may appear that the overall computational workload increases due to the need to repeatedly assess the error at each step, in practice, when the solution to the equations undergoes significant variation, the total computational effort is reduced, and the error is effectively controlled. The nonlinear dynamics equations of the transmission system are solved using the fourth-order Runge-Kutta method with adaptive step size, yielding the maximum torsional displacement of each degree of freedom in the system, as shown in Fig. 6.

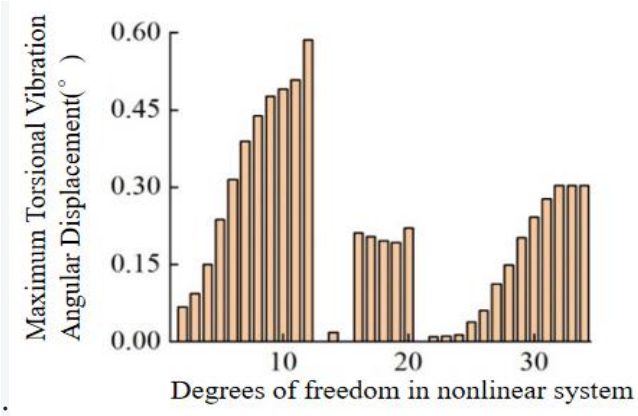

Figure 6 Maximum torsional angular displacement of freedom degree

As can be seen from the above figure, the amplitude of torsional vibration of the transmission system of the equipment on the fracturing truck platform is the largest at the output end of the engine, followed by the free end of the fracturing pump. The torsional vibration response curves of the engine output and the free end of the fracturing pump are shown in Fig. 7 and 8.

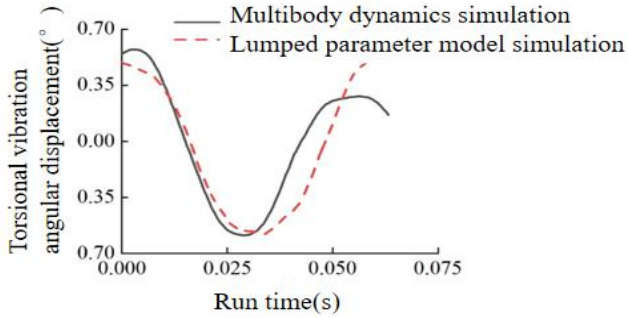

Figure 7 Response curve of engine output

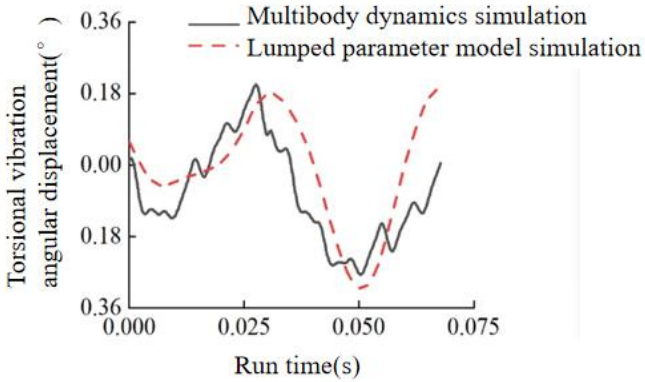

Figure 8 Response curve of free end of pump

The maximum torsional angle of the transmission system, obtained using the Runge-Kutta method, is 0.5863°, which deviates by 2.4% from the value obtained through multibody dynamics. A comparison shows that the response curve of the nonlinear transmission system model, solved via the Runge-Kutta method, generally follows the trend of the multibody dynamics model solved with ADAMS, though some error exists. The primary sources of error include:

a) The nonlinear system model simplifies the transmission system, neglecting the impact of its geometric shape on the torsional vibration response.

b) The ADAMS multibody dynamics simulation, while using boundary conditions close to real supports, does not account for the influence of the other five degrees of freedom on the torsional vibration response.

c) Errors are introduced during the flexible modeling process in multibody dynamics due to mesh partitioning, the addition of output interfaces, and filtering of higher-order modes.

d) The inclusion of nonlinear parameters, while improving the realism of the results, introduces cumulative errors in the numerical solution process.

According to the petroleum and natural gas industry standard SY/T 5211-2009, the torsional vibration amplitude of fracturing equipment shaft systems should not exceed 0.5°. Therefore, further research into torsional vibration control for this system is essential.

4 Qualitative analysis of nonlinear systems

In the study of nonlinear systems, merely using quantitative analysis to derive the response curves does not provide a clear representation of the system's response characteristics. A qualitative analysis is also necessary to determine the system's stability and periodic behavior.

Taking the structural damping of a transmission system as the research subject, this study investigates the effect of varying damping coefficients on the system's torsional vibration response. A bifurcation diagram is plotted for the system's damping coefficient in the range of [0, 0.05], as shown in Fig. 9. According to the bifurcation diagram, when the damping coefficient is zero, the system exhibits chaotic motion. As the damping coefficient increases, the system stabilizes and transitions to a single-periodic oscillation state.The periodic characteristics of the system are further analyzed for damping coefficients of 0 and 0.035, respectively, to explore the impact of damping on the system's dynamic response.

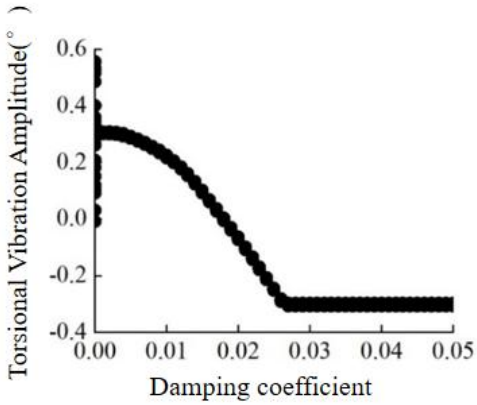

Figure 9 **System bifurcation diagram of damping coefficient**

When the system's damping coefficient is zero, the Poincaré section is plotted based on the phase plane diagram, with the initial section set at zero. The torsional vibration response curve, phase plane diagram, and Poincaré section diagram of the engine crankshaft output are shown in Fig. 10. Similarly, the torsional vibration response curve, phase plane diagram, and Poincaré section diagram of the fracturing pump crankshaft output are also depicted in the same figure.

It can be observed that the phase diagram of the engine crankshaft output consists of intercrossing, closed-loop trajectories, and in the Poincaré section diagram, it appears as three distinct cloud-like point clusters, indicating a quasi-periodic motion with a 3-period cycle. In contrast, the phase plane diagram of the free end of the fracturing pump exhibits intersecting, non-coincident, and unstable trajectories, with the Poincaré section showing multiple point clusters, reflecting a non-periodic chaotic response.

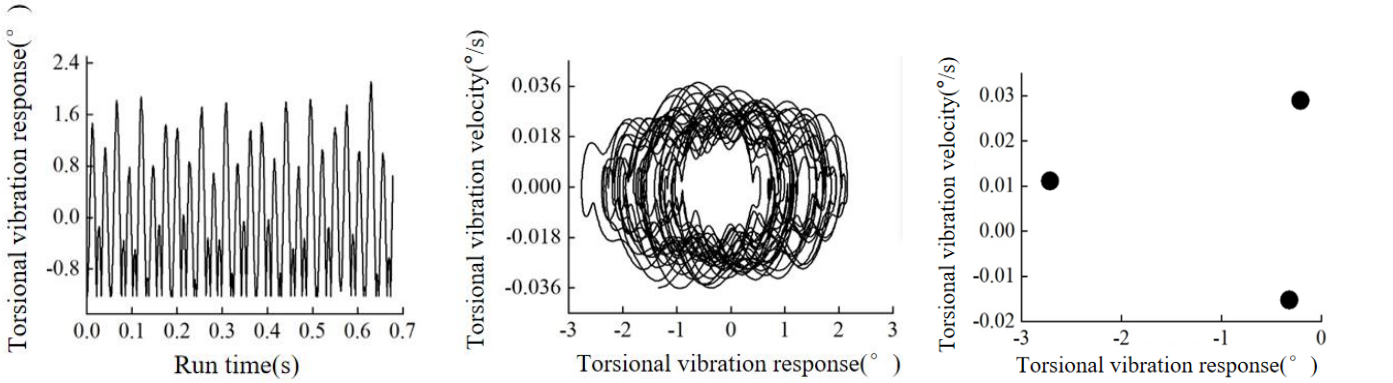

a. Engine crankshaft output shaft engine torsional vibration response diagram **b. Engine crankshaft output shaft phase plane diagram** **c. Poincaré section diagram of the crankshaft output shaft**

Fig.10 Analysis results of engine crankshaft output(when the system damping factor is 0)

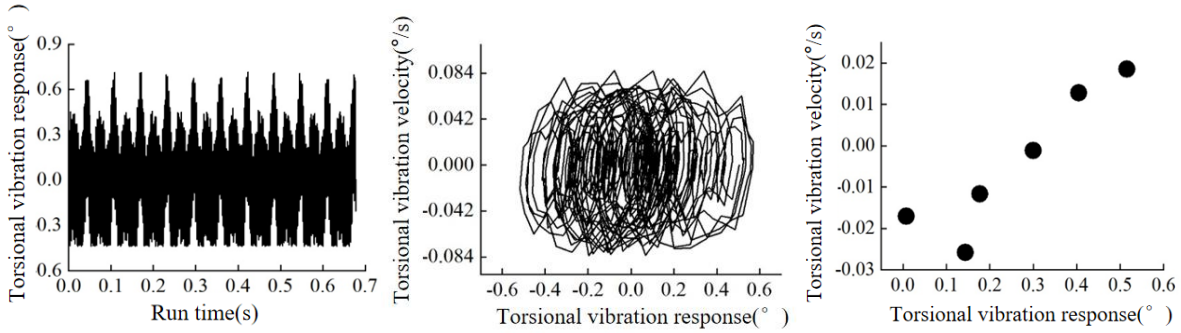

a. Fracturing pump crankshaft output b. Fracturing pump crankshaft c. Fracturing pump crankshaft

shaft torsional vibration response diagram output shaft phase plane diagram output shaft Poincaré section diagram

Figure 11 Analysis results of fracturing pump crankshaft outputs(when the system damping factor is 0)

When the damping coefficient is 0.035, the Poincare section diagram is drawn based on the phase plane diagram, with the initial section set at zero. The torsional vibration response curves, phase plane diagrams, and Poincare section diagrams of both the engine crankshaft and the fracturing pump crankshaft outputs are shown in Figures 12 and 13.

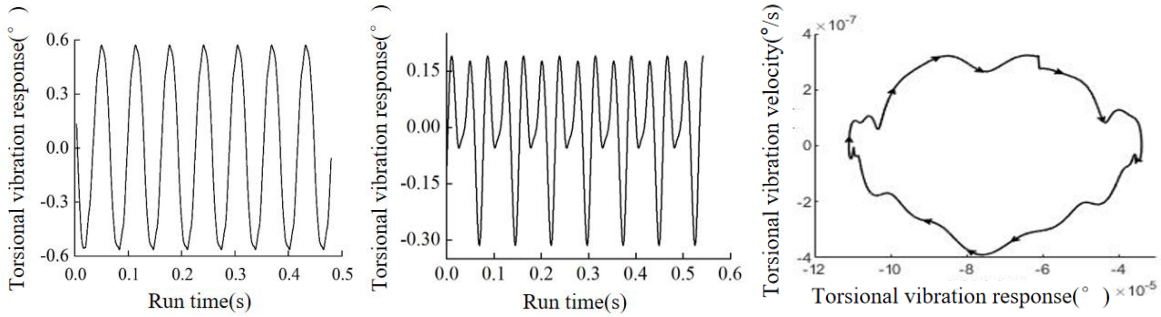

a. Engine crankshaft output shaft torsional vibration response diagram b. Engine crankshaft output shaft phase plane diagram c. Engine crankshaft output shaft Poincaré section diagram

Figure 12 Analysis results of engine crankshaft output (when the system damping factor is 0.035)

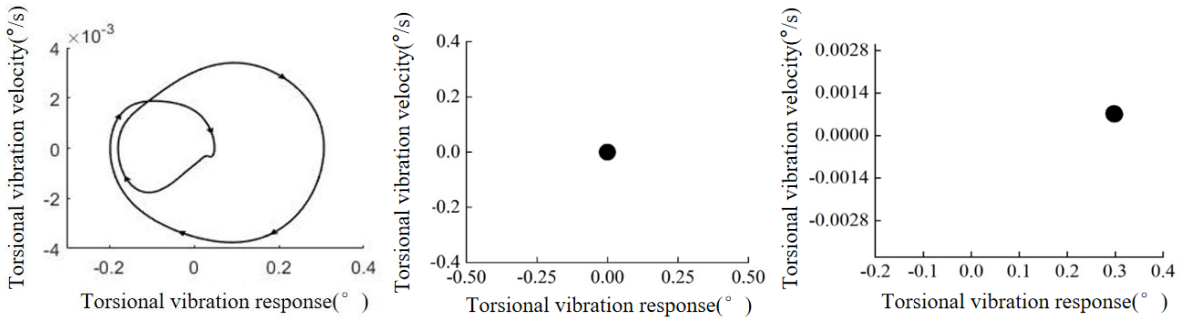

a. Fracturing pump crankshaft output shaft torsional vibration response diagram b. Fracturing pump crankshaft output shaft phase plane diagram c. Fracturing pump crankshaft output shaft Poincaré section diagram

Figure 13 Analysis results of fracturing pump crankshaft outputs

(when the system damping factor is 0.035)

From the above diagram, it can be concluded that both the phase diagrams of the engine crankshaft output and the free end of the fracturing pump show stable closed loops, indicating that the response tends to stabilize. Additionally, the Poincar**é** section diagrams exhibit a single-point state, which indicates that the response is a periodic, single-cycle response.

5 Conclusion

In this study, a nonlinear dynamic equation for the drive system of the fracturing vehicle is established by analyzing multiple nonlinear parameters of the equipment transmission system. The system's torsional vibration response at critical positions is solved numerically using the adaptive step-size fourth-order Runge-Kutta method. By comparing the obtained response curves with those from simulation methods, it is found that while there are some numerical errors, the overall trends of the two results are consistent. A qualitative analysis of the nonlinear system is conducted using graphical methods, resulting in the bifurcation diagram, phase plane diagram, and Poincaré section diagram. It is concluded that when damping is neglected, the torsional vibration response of the drive system exhibits a non-periodic chaotic behavior. However, when damping is considered, the system's torsional vibration response stabilizes and transitions to a stable, single-periodic state.

Reference

1. L Shuang, A Hongling, L Zhenjun, et al. Analysis of vibration characteristics and adaptive continuous perturbation control of some torsional vibration system with backlash [J]. Chaos, Solitons and Fractals: The Interdisciplinary Journal of Nonlinear Science, and Nonequilibrium and Complex Phenomena, 2017, 103.
2. L Liping, L Zhaijun, L Xue-Lai, et al. Modeling and analysis of friction clutch at a driveline for suppressing car starting judder[J]. Journal of Sound and Vibration, 2018, 424.
3. W Siyu, Z Rupeng, S Shuaishuai. Nonlinear Torsional Dynamics of Star Gearing Transmission System of GTF Gearbox[J]. Shock and Vibration, 2020, 2020.
4. Qu J, Shi W, Wang J, et al. Modeling and analysis of clutch nonlinear behavior in an automotive driveline for suppressing torsional vibration[J]. Machines, 2022, 10(9): 819.
5. Moharrami M J, de Arruda Martins C, Shiri H. Nonlinear integrated dynamic analysis of drill strings under stick-slip vibration[J]. Applied Ocean Research, 2021, 108: 102521.
6. Xia Y, Chu Z, Pang J. Modelling and application of typical nonlinear torsional elements in vibro-impact analysis of pickup truck driveline system[J]. Journal of Sound and Vibration, 2024: 118561.
7. Xia Y, Pang J, Yang L, et al. Investigation on clearance-induced vibro-impacts of torsional system based on Hertz contact nonlinearity[J]. Mechanism and Machine Theory, 2021, 162: 104342.
8. Xia Y, Pang J, Yang L, et al. Nonlinear numerical and experimental study on the second-order torsional and lateral vibration of driveline system connected by cardan joint[J]. Journal of Vibration and Control, 2020, 26(7-8): 540-551.
9. Idehara S J, Flach F L, Lemes D. Modeling of nonlinear torsional vibration of the automotive powertrain[J]. Journal of Vibration and Control, 2018, 24(9): 1774-1786.
10. He L, Xia C, Chen S, et al. Parametric Investigation of Dual-Mass Flywheel Based on Driveline Start-Up Torsional Vibration Control[J]. Shock and Vibration, 2019, 2019 (1): 3171698.
11. Liu C, Zhou C, Tan L, et al. Reliability analysis of subsea manifold system using FMECA and FFTA[J]. Scientific Reports, 2024, 14(1): 22873.
12. Wu L, Yang Y, Maheshwari M. Strain prediction for critical positions of FPSO under different loading of stored oil using GAIFOA-BP neural network[J]. Marine Structures, 2020, 72: 102762.
13. Wu L, Mei J, Zhao S. Pipeline damage identification based on an optimized back-propagation neural network improved by whale optimization algorithm[J]. Applied Intelligence, 2023, 53(10): 12937-12954.
14. Liu C, Li G, Xiao W, et al. Reliability analysis of subsea control system using FMEA and FFTA[J]. Scientific Reports, 2024, 14(1): 1-21.
15. Xiao W.S, Li G.X., Liu C., et al. A novel chaotic and neighborhood search-based artificial bee colony algorithm for solving optimization problems [J]. Scientific Reports, 2023, 13(1): 20496.
16. Liu, C., Wu, L., Huang, X.D., Xiao, W.S. Improved dynamic adaptive ant colony optimization algorithm to solve pipe routing design [J]. Knowledge-based systems, 2022, 237: 107846.
17. Li G.X, Liu C., Xiao W.S, et al. A mixing algorithm of ACO and ABC for solving path planning mobile robot [J]. Applied Soft Computing Journal, 2023, 148: 110868.
18. Liu, C., Wu, L., Xiao, W.S., et al. An improved heuristic mechanism ant colony optimization algorithm for solving path planning[J]. Knowledge-Based Systems, 2023, 271: 110540.
19. Liu, C., Wu, L., Li, G.X., H, Zhang, Xiao, W.S, Xu, D.P., Guo, J.J. Improved multi-search strategy A* algorithm to solve three-dimensional pipe routing design [J]. Expert Systems with Applications, 240 (2024), Article 122313.
20. Liu C, Wu L, Li G, et al. AI-based 3D pipe automation layout with enhanced ant colony optimization algorithm[J]. Automation in Construction, 2024, 167: 105689.